NUMERICAL SIMULATION OF A STRAINED TURBULENT AXIAL VORTEX

Gregory A. Blaisdell
Jim H. Qin
School of Aeronautics and Astronautics
Purdue University
West Lafayette, Indiana 47907-1282, USA

ABSTRACT

Direct numerical simulations of a turbulent axial vortex are performed both with and without an externally applied strain field. The global behavior of the turbulence and detailed profiles are examined. Without strain, the turbulence shows transient growth, but ultimately it decays as the flow is stabilized. Simulations with strain are able to capture the instability due to strain only for cases with an axial flow and sufficiently high Reynolds numbers.

INTRODUCTION

Results are presented from a numerical study of a turbulent axial vortex including the effects of an external strain field. This work is motivated by the wake hazard problem for commercial aircraft where the wingtip vortices behind large aircraft present a serious safety concern for following aircraft. In order for progress to be made in the prediction and control of these vortices it will be helpful to have a better understanding of how turbulence within these vortices behaves and how the turbulence affects the distribution of vorticity. The effect of strain is included because each vortex of a trailing vortex pair induces a strain field on the opposite vortex. The strain creates an instability which affects the development of turbulence within the vortex.

There have been several experimental studies of turbulent vortices, which are discussed in the papers by Devenport et al. (1996) and Leweke and Williamson (1998). Numerical simulations of an isolated turbulent axial vortex have been presented in a series of papers by Ragab and Sreedhar (1995). Recently Orlandi et al. (1998) have simulated a pair of turbulent vortices corresponding to the experiments of Leweke and Williamson. The objective of the current study is to help improve our understanding of the turbulent axial vortex and its response to strain.

ISOLATED VORTEX

The vortex under consideration is time-developing and, therefore, homogeneous in the axial (z) direction. This corresponds to a vortex far downstream, under the approximation that the flow changes slowly in the streamwise direction.

Numerical Method

The computer code used for the isolated vortex simulations (i.e. without strain) is a modified version of the code of Blaisdell et al. (1993) for simulating compressible homogeneous turbulence. The compressible Navier-Stokes equations are solved; however, the Mach numbers are low, and compressibility effects are insignificant, as is verified by noting that the density varies by less than 2%.

The code uses a Fourier spectral method with periodic boundary conditions in all three directions. To avoid the undesirable influence of image vortices, a coordinate mapping due to Cain et al. (1984) is used in the x and y directions to move the periodic boundaries to infinity. More detail about the numerical method can be found in Blaisdell et al. (1993) and Qin (1998).

Simulations

The initial mean velocity field is that of the q-vortex (Ragab and Sreedhar, 1995), which includes an axial wake flow, and is given by

$$\frac{V_\theta}{V_0} = \frac{q_0}{\hat{r}}(1 - e^{-\hat{r}^2}) \tag{1}$$

$$\frac{V_z}{V_0} = (1 - e^{-\hat{r}^2}) \tag{2}$$

where V_0 is the magnitude of the wake flow, $\hat{r} = \gamma r/r_0$, r_0 is the location of the peak tangential velocity, the constant γ is the root of $1 + 2\gamma^2 = e^{\gamma^2}$, and q_0 is the initial swirl number. The initial mean tangential and axial velocity is shown in figure 1. The initial turbulent velocity field consists of small amplitude random disturbances with a specified intensity profile. Two types of disturbance profiles are used. The first is a Gaussian profile and the second has its peak disturbance in an annular region, as shown in figure 2. Also cases are run with high and low disturbance levels using each of these profiles. The parameters for the simulations run are shown in table 1. All the simulations were done at a Reynolds number $Re = \Gamma_\infty/\nu = 16500$. The computational grid used had $N_x \times N_y \times N_z = 128 \times 128 \times 256$, except for Case B, which has a $256 \times 256 \times 128$ grid on a domain that is half as long. Case F does not include any mean axial flow. For case A, an ensemble of four simulations using different random initial disturbances were run in order to obtain high-quality statistics.

Results and Discussion

One can get a global sense of the stability of the flow by considering the global turbulent kinetic energy (volume averaged turbulent kinetic energy within a radius $R = 5r_0$). This is plotted in figure 3. Time is nondimensionalized by $T = 2\pi r_0/V_\theta(r_0, 0)$. The initial value of q is such that the flow is unstable and so the global turbulent kinetic energy grows. As pointed out by Ragab and Sreedhar (1995), the wake magnitude decays in time which eventually stabilizes the flow. Therefore, the global turbulent kinetic energy reaches a peak and then decays in time.

The behavior is qualitatively the same regardless of the type of initial disturbance profile or the level of the initial disturbance. In fact if the time axis is shifted appropriately the curves line up with one another, as shown in figure 4. Here the data is plotted on semi-log axes so the region of exponential grown can be clearly seen. Because of the similarity in the behavior of the simulations, only case A will be considered further in examining the isolated vortex simulations.

The mean axial velocity is shown in figure 5. At early times the wake profile changes slowly, until the turbulence has a chance to develop. The wake then decays, as one would expect. The mean tangential velocity is given in figure 6. It shows decay of the peak velocity and an outward motion of the location of the peak, as one would expect. However, at later times, when the flow is stabilized, the location of the peak velocity moves inward. Therefore, the vortex displays an anti-diffusive behavior. Also note that the mean tangential velocity close to the vortex center initially decreases and then increases at later times. Usually one thinks of turbulence gaining energy from the mean flow; however, here is a case where, during the stabilized period, as the turbulence decays, the turbulence gives energy to the mean flow and strengthens it.

The circulation is given by $\Gamma(r) = 2\pi r V_\theta$. Its initial profile has a monotonicly increasing circulation, which indicates that the case without any axial velocity is stable according to Rayleigh's criterion. The circulation profile (not shown) develops a very slight circulation overshoot, which moves outward in time. However, the region of decreasing circulation does not seem to give rise to an instability.

The evolution of the profiles of turbulent kinetic energy (TKE) is shown in figure 7. Initially the TKE has a Gaussian shape and a low amplitude. The turbulence grows in an annular region, peaked near the location of the inflection point in the mean axial velocity profile. When the flow becomes stabilized the peak in the TKE moves to the centerline, and the amplitude decays.

The Reynolds shear stresses are shown in figures 8-10. The Reynolds stresses generally grow and decay with the TKE. The stresses $\overline{v_r' v_z'}$ and $\overline{v_\theta' v_z'}$ remain fairly compact in their distribution; however, the shear stress $\overline{v_r' v_\theta'}$ continues to spread outward at later times, and the location of the peak seems to match the location of the circulation overshoot. At later times the Reynolds shear stresses develop a region near the center of the vortex where the sign of the stress changes. As will now be shown, this is associated with the anti-diffusive behavior discussed earlier.

The eddy viscosity, defined by

$$\nu_T = -\frac{\overline{v_r' v_\theta'} S_{r\theta} + \overline{v_r' v_z'} S_{rz}}{2(S_{r\theta}^2 + S_{rz}^2)} \tag{3}$$

where S_{ij} is the mean strain rate tensor, is plotted in figure 11. We see that the eddy viscosity becomes much greater than the molecular viscosity. At later times ν_T becomes negative near the center of the vortex. This is where the anti-diffusion of the mean velocity field occurs.

Figure 12 shows a visualization of the vortex at a time when the TKE is near its peak. (This visualization is actually taken from a test case using the b-spline code mentioned in the next section.) The vortex develops helical vortex structures, which correspond to the dominant instability modes. As the turbulence decays, the helical vortex structures slowly disappear and the peak vorticity magnitude moves to the vortex center.

VORTEX WITH STRAIN

As we have seen above, the isolated vortex becomes stable and ultimately the turbulence decays. For a pair of vortices, as in the wake of an airplane, each vortex induces a strain field on the other vortex. The strain gives rise to an instability in which the long-wavelength modes are known as the Crow instability (Crow, 1970) and the short-wavelength modes are known as the Wid-

nall instability (Widnall et al., 1974). In order to determine the effect of externally applied strain on the development of turbulence within the vortex, a model problem is solved in which the vortex is subjected to a uniform strain field. The principle axes of the strain are in the x and y directions. The compressible code used for the first part of this study will not work with an added strain field. Therefore, it was necessary to use a different numerical method for the strained vortex simulations.

Numerical Method

The computer program used for the strained vortex calculations was originally developed by Loulou (1996) to study turbulent pipe flow. It solves the incompressible equations in cylindrical coordinates using a Galerkin formulation with a spectral Fourier method in z and θ and a b-spline method in r. The code has been modified to run on an IBM SP parallel computer. A detailed description of the numerical method is given in Qin (1998).

Simulations

A table of the run parameters is given in table 2. Two of the simulations included an axial flow and two did not. The effect of varying the Reynolds number was also examined. The parameter $\beta = e/\gamma^*$, where e is the strain rate and $\gamma^* = \Gamma_\infty/(2\pi r_0^2)$. The grid used for the simulations with strain is $N_z = 192$, $N_\theta^{max} = 96$, $N_r = 128$.

Results and Discussion

The global TKE histories for the two cases with strain, but with no axial flow, are shown in figure 13 compared to a case with no strain and no axial flow. The case without strain shows simple decay, since the flow is stable for all time. The cases with strain show a transient growth period; however, they ultimately decay. The simulation STRN4, which is run at a higher Reynolds number, shows a higher level of turbulence developing. We believe the reason the simulations show eventual decay is that the Reynolds number is too low. Reynolds number is important to capturing the instability due to strain, as is pointed out in the analysis of the related elliptic streamline flow by Landman and Saffman (1987) (and others) and the homogeneous turbulence simulations of Blaisdell and Shariff (1996).

The evolution of the global TKE for the cases with strain and an axial velocity are compared in figure 14 to two cases without strain, which use the two different computer codes. The difference between the "Spectral" (compressible) results and the b-spline results is a delay in the development of the turbulence due to differences in the initial fluctuations. The cases with strain follow the results for the case without strain through the linear growth stage. However, the cases with strain continue to show growth for a longer period of time. The low Reynolds number strained simulation eventually decays. However, the higher Reynolds number case, STRN2, seems to have captured the instability and shows sustained growth. Case STRN2 also had a higher nondimensional strain rate in an effort to capture the instability.

With strain the vortex in no longer axisymmetric, so it is more difficult to gather and analyze statistics. Isocontours of the TKE averaged in the axial direction (not shown) during the latter stages of growth in case STRN2 show that the peak lies off the vortex axis.

There is a significant difference in the Reynolds stresses between the case with strain and the case without strain. A contour plot of the $\overline{v_r' v_z'}$ Reynolds stress (averaged in z) is shown in figure 15 for case STRN2. Here one can see the development of regions of large positive stress whereas the cases without strain shown in figure 9 has a stress that remains negative except for a region close to the vortex center that has small positive values.

CONCLUSIONS

Simulations of a turbulent axial vortex have been performed with and without an externally applied strain field. Both the global behavior of the turbulence and detailed profiles are examined. Without strain the turbulence shows transient growth, but ultimately decays as the flow is stabilized. Simulations with strain, but without an axial flow, showed only transient growth, which is believed to be due to the limitation of low Reynolds numbers. Simulations with strain and axial flow showed transient growth of the turbulence at low Reynolds numbers, but sustained growth at higher Reynolds numbers. The instability due to strain seems to be easier to capture in the presence of a mean axial flow.

ACKNOWLEDGMENTS

This work was supported in part by the Purdue Research Foundation and the IBM SUR program. The computations were done using the Intel Paragon and IBM SP at the Purdue University Computing Center.

REFERENCES

Blaisdell, G. A., Mansour, N. N., and Reynolds, W. C., 1993, "Numerical simulations of compressible homogeneous turbulence," *J. Fluid Mech.*, Vol. 256, pp. 443–485.

Blaisdell, G. A. and Shariff, K., 1996, "Simulation and modeling of the elliptic streamline flow," *Proceedings of the Summer Program*, Center for Turbulence Research, Stanford/NASA Ames, pp. 433–446.

Cain, A. B., Ferziger, J. H., and Reynolds, W. C., 1984, "Discrete orthogonal function expansions for non-uniform grids using the fast Fourier transform," *J. Comp. Phys.*, Vol. 56, pp. 272–286.

Crow, S. C., 1970, "Stability theory for a pair of trailing vortices," *AIAA Journal*, Vol. 8, pp. 2172–2179.

Devenport, W. J., Rife, M. C., Liapis, S. I. and Follin, G. J., 1996, "The structure and development of a wing-tip vortex," *J. Fluid Mech.*, Vol. 312, pp. 67–106.

Landman, M. J. and Saffman, P. G., 1987, "The three-dimensional instability of strained vortices in a viscous fluid," *Phys. Fluids*, Vol. 30, pp. 2339–2342.

Leweke, T. and Williamson, C. H. K., 1998, "Cooperative elliptic instability of a vortex pair." *J. Fluid Mech.*, Vol. 360, pp. 85–119.

Loulou, Patrick, 1996, "Direct Numerical Simulation of Incompressible Pipe Flow Using a B-Spline Spectral Method," Ph.D. thesis, Department of Aeronautics and Astronautics, Stanford University, June 1996.

Orlandi, P., Carnevale, G. F., Lele, S. K., and Shariff, K., 1998, "DNS study of stability of trailing vortices," *Proceedings of the Summer Program*, Center for Turbulence Research, Stanford/NASA Ames, pp. 187–208.

Qin, J. H., 1998, "Numerical simulations of a turbulent axial vortex," Ph.D. thesis, School of Aeronautics and Astronautics, Purdue University, December 1998.

Ragab, S. A. and Sreedhar, M. K., 1995, "Numerical simulation of vortices with axial velocity deficits," *Phys. Fluids*, Vol. 7, pp. 549–558.

Widnall, S. E., Bliss, D. B., and Tsai, C.-Y., 1974, "The instability of short waves on a vortex ring," *J. Fluid Mech.*, Vol. 66, pp. 35–47.

Table 1: Case parameters for the isolated axial vortex.

Case	Dist. level	Dist. profile
A	low	Gaussian
B	low	Gaussian
C	high	Gaussian
D	high	annular
E	low	annular
F	low	Gaussian

Table 2: Case parameters for the strained vortex.

Case	β	$Re = \Gamma_\infty/\nu$	Axial flow
STRN1	0.0281	19268	wake
STRN2	0.0404	29428	wake
STRN3	0.0404	29428	none
STRN4	0.0404	58836	none

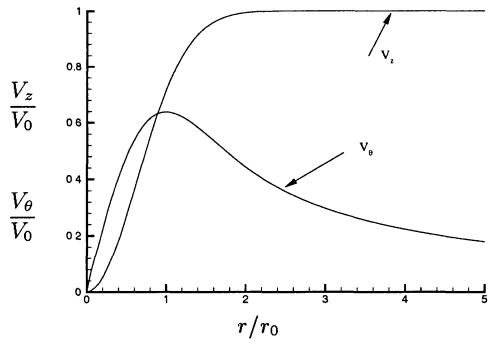

Figure 1: The initial mean velocity profiles.

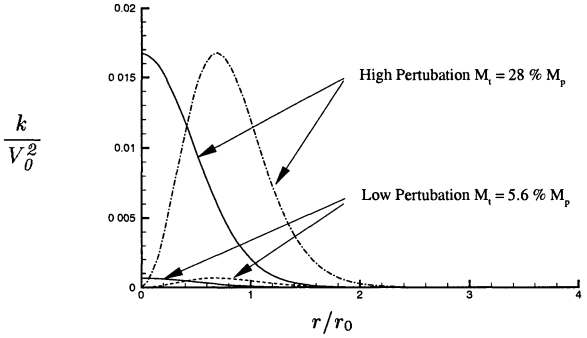

Figure 2: Profiles of the initial turbulent kinetic energy.

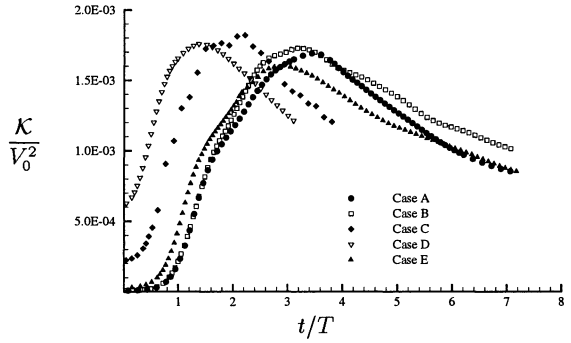

Figure 3: Evolution of the global TKE $\mathcal{K}$ for five cases.

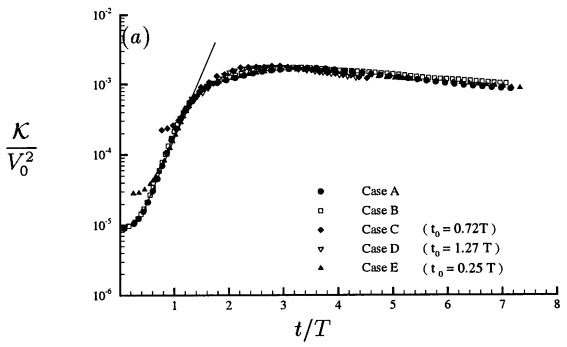

Figure 4: The evolution of the global TKE shifted by time t_0.

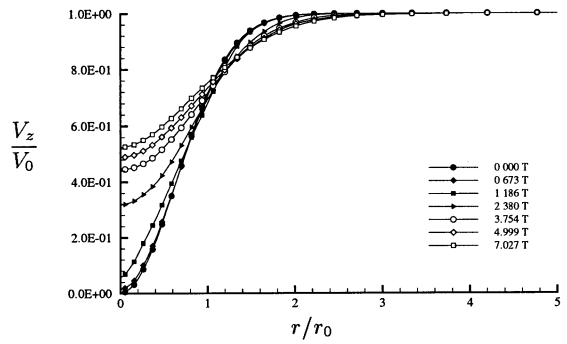

Figure 5: Evolution of the mean axial velocity V_z profiles for Case A.

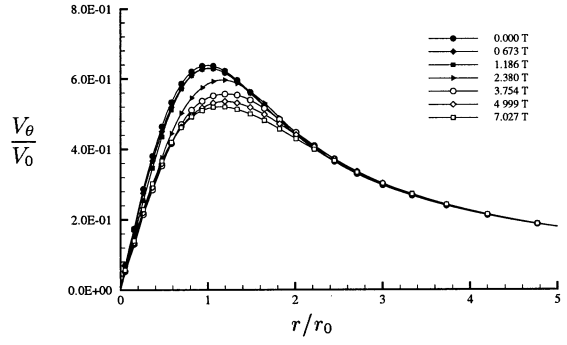

Figure 6: Evolution of the mean tangential velocity V_θ profiles.

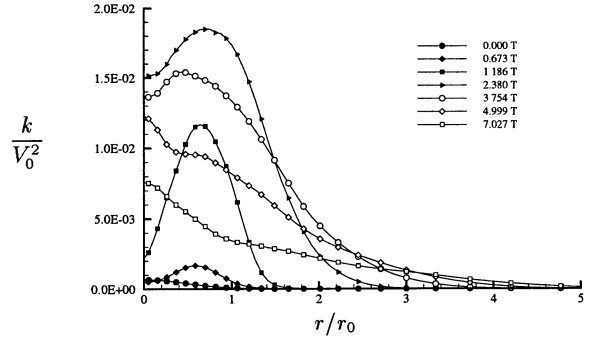

Figure 7: Evolution of the TKE k profiles.

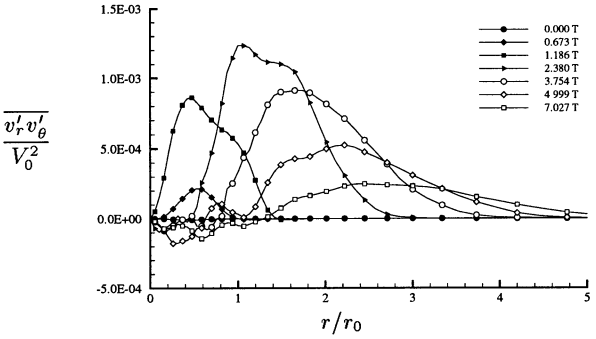

Figure 8: Evolution of Reynolds stress $\overline{v_r' v_\theta'}$ profiles.

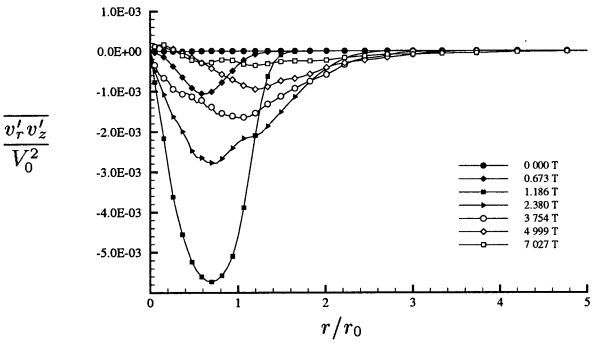

Figure 9: Evolution of the Reynolds stress $v_r' v_z'$ profiles.

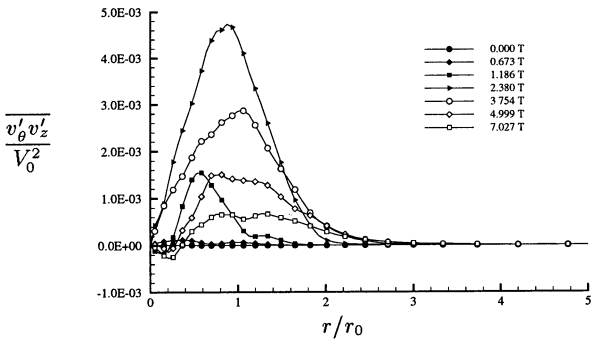

Figure 10: Evolution of Reynolds stress $\overline{v'_\theta v'_z}$ profiles.

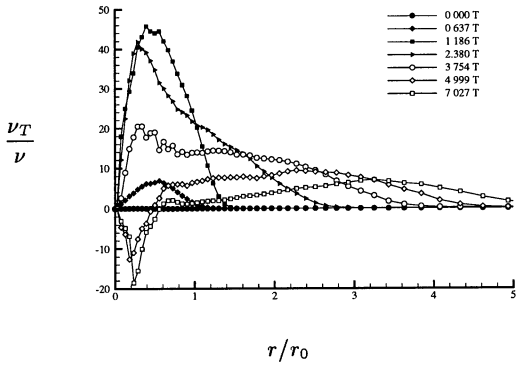

Figure 11: Evolution of the eddy ν_T/ν profiles.

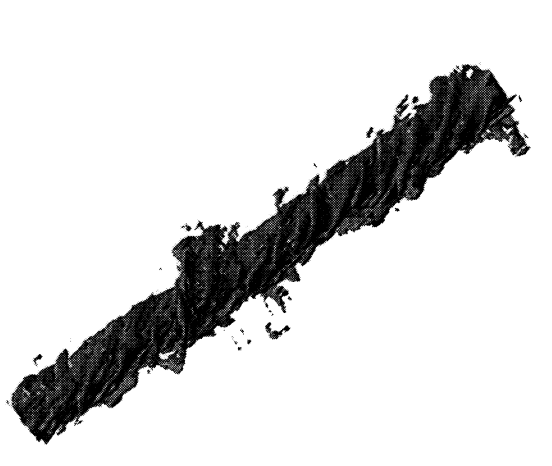

Figure 12: Isosurfaces of vorticity magnitude for $t = 4.4T$.

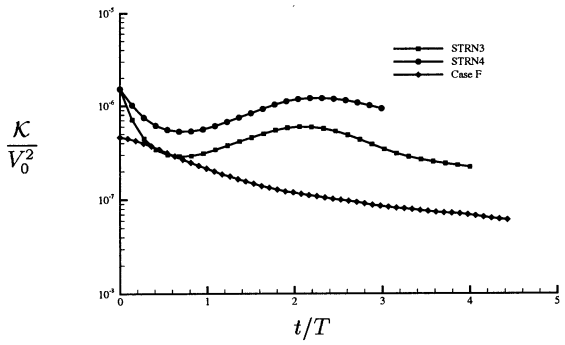

Figure 13: The evolution of the Global TKE of the strained Oseen vortex.

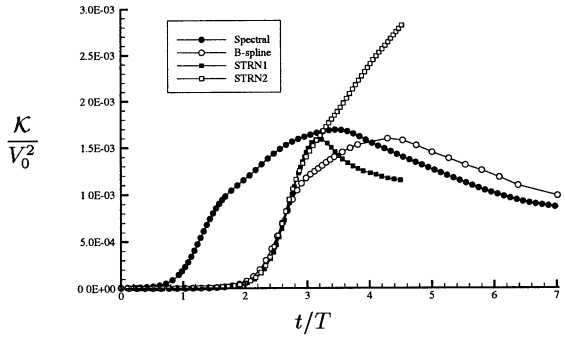

Figure 14: The evolution of the Global TKE of the strained vortex.

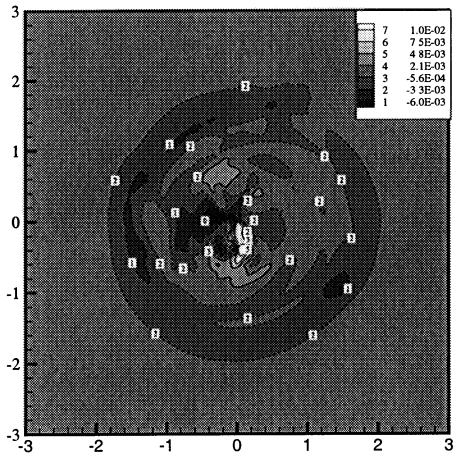

Figure 15: Contours of $\overline{v'_r v'_z}$ at $t = 3.30T$.